



Three-Dimensional Characterization of Active Membrane Waves on Living Cells

Chien-Hong Chen,¹ Feng-Ching Tsai,² Chun-Chieh Wang,² and Chau-Hwang Lee^{1,2,*}

¹*Institute of Biophotonics, National Yang-Ming University, 155 Sec. 2, Linong Street, Taipei 11221, Taiwan*

²*Research Center for Applied Sciences, Academia Sinica, 128 Sec. 2, Academia Road, Taipei 11529, Taiwan*

(Received 22 July 2009; published 30 November 2009)

We measure the temporal evolution of three-dimensional membrane topography on living fibroblasts and characterize the propagation of membrane waves using a wide-field optical profiling technique. The measured membrane profiles are compared with the numerical results calculated by the active membrane model recently proposed by Shlomovitz and Gov. After the treatments of blebbistatin and latrunculin A separately, the membrane waves disappear and the membrane surfaces are flattened, verifying that the membrane waves are driven by the interactions between myosin II and actin polymerization.

DOI: 10.1103/PhysRevLett.103.238101

PACS numbers: 87.16.Gj, 87.16.dj, 87.17.Jj, 87.64.-t

Membrane waves or ripples of living cells have been studied intensively in recent years [1–10]. These waves are believed to be driven by the interactions of motile proteins such as actin and myosin associated with membranes [8,9]. A study performed on mouse embryonic fibroblasts, fly wing disk cells, and mouse *T* cells concludes that for these three kinds of cells the lateral speeds of membrane waves are on the order of 100 nm/sec [6]. Shlomovitz and Gov have calculated that the amplitudes of membrane waves would be about 100 nm with wavelengths of a few micrometers [10]. Apparently conventional optical microscopy techniques cannot resolve the three-dimensional (3D) topographic features of membrane activities in this scale. Some advanced microscopy techniques such as diffraction phase microscopy [11] or defocusing microscopy [12] can be utilized to analyze the thicknesses and dynamics of living cells. However, the information from optical path differences requires the knowledge about refractive indices in the cytoplasm for correct interpretations of cell thicknesses.

In this Letter we report 3D characterizations of membrane waves by using an optical profiling technique with nanometer depth sensitivity called noninterferometric wide-field optical profilometry (NIWOP) [13]. With systematic analyses on the kymographs of the membrane topography, we reveal the propagation features of the amplitudes, wavelengths, and speeds of membrane waves. We also obtain the dispersion relation and the frequency response of amplitudes. These characterizations are compared with the model of active membrane waves proposed by Shlomovitz and Gov [9,10]. In addition, we treat the cells with drugs that inhibit actin-filament elongation or suppress myosin II activities, and verify that the generation of membrane waves requires both actin polymerization and myosin activities.

The working principle of NIWOP is based on two techniques: wide-field optical sectioning microscopy [14] and differential confocal microscopy [15]. With the axial response curve provided by the wide-field sectioning microscopy, we obtain nanometer depth sensitivity by placing the

sample surface into the linear region of the axial response curve. This principle of NIWOP is illustrated in Fig. 1(a) with the axial response curve obtained by a $60\times$, 1.2 NA water-immersion objective. For the calibration of membrane heights, we consider the lamellipodium of a cell as a dielectric layer of nonuniform refractive indices and thicknesses. Then we obtain these two parameters on each pixel by combining the intensity values acquired as the specimen placed in the linear region and from the conventional bright-field image. Typical depth profiling accuracy on living cell membranes is about 20 nm. Details about the applications of NIWOP to cell membrane profiling can be found in our previous publications [5,7,16]. In the present work the acquisition rate of NIWOP topography is 12 frames/min.

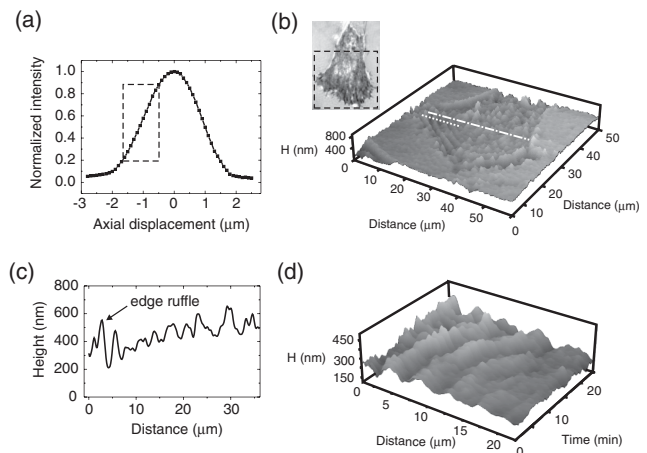


FIG. 1. (a) Axial response curve of wide-field optical sectioning microscopy. A dashed rectangle indicates the working region of NIWOP. (b) Typical membrane topography obtained by NIWOP. The inset shows the bright-field reflection image of this cell and the dashed square labels the observation area. (c) Membrane-height profile along the dash-dot line in (b). (d) Kymograph of the membrane topography along the dashed line in (b). On the distance axis, the origin represents the cell edge.

The experiments were conducted on HS68 fibroblasts. The cells were cultured in Dulbecco's Modified Eagle's Medium (DMEM) supplemented with 10% fetal bovine serum and 1% antibiotic pen-strep-ampho. Before the observation, we replaced the culture medium by phenol-red-free DMEM to reduce the optical absorption of the medium and to improve the contrast of images. During the experiments the culture medium containing the cells was kept at $37^\circ \pm 0.1^\circ\text{C}$.

Figure 1(b) shows a typical cell membrane topography obtained by NIWOP. Because a single reflection surface such as the dish bottom does not fit our model for membrane-height calibrations, the cell surface in Fig. 1(b) looks lower than the surrounding dish bottom. Nonetheless, for characterizing the membrane waves we only use the membrane heights on cell surface. We also show the membrane-height profile in Fig. 1(c). For this cell, the extension of lamella gradually reduces the membrane height, and the edge ruffle is clear. The kymograph in Fig. 1(d) is recorded along the dashed line in Fig. 1(b), where concentric membrane waves are clear. This kymograph shows a membrane wave propagating away from the protruding edge to the cell center. The amplitudes gradually decrease during this centripetal propagation. The result in Fig. 1(d) resembles that calculated from the active membrane wave model considering a line of oscillating force at the origin of the distance axis [10], suggesting that the driving source of the retrograde propagating membrane waves would be at the cell edge, such as edge ruffles [4,8].

We identify propagating membrane waves on 23 cells, and plot the variations of peak-to-valley amplitudes and wavelengths along with the distances to cell edges in Fig. 2. Because of the lateral extension of membrane waves, we may have several measurements of amplitudes and wavelengths at a specific distance on one cell. We use the Student's t distribution to determine the 95% confidence interval of each data point, shown as the error bars. In Fig. 2(a) we find that the amplitudes are around 240 nm near the cell edges. The amplitudes increase to about 300 nm at a distance of $9\ \mu\text{m}$, and then decrease to nearly 130 nm with a propagation distance of $31\ \mu\text{m}$. As the membrane waves propagate into the central areas of cells, the absorption and scattering in cytoplasm become significant and our dielectric-layer model of membrane-height calibration cannot provide correct thicknesses [5]. Hence we are not able to track the wave peaks to the positions where they completely disappear. On the basis of the mechanism proposed by Giannone *et al.* [8], the formation of membrane waves requires focal adhesions near cell edges. That explains why the amplitudes do not reach the maximum at the edge. A second feature is that the wavelengths increase during the centripetal propagation, as shown in Fig. 2(b). We use an exponential growth form $\lambda(x) = \lambda_a[1 - \exp(-x/x_c)]$ to depict the change of the wavelength λ along the propagation distance x . With curve fitting we find that the asymptotic steady-state wavelength $\lambda_a = 4.9\ \mu\text{m}$, and the characteristic growth distance $x_c =$

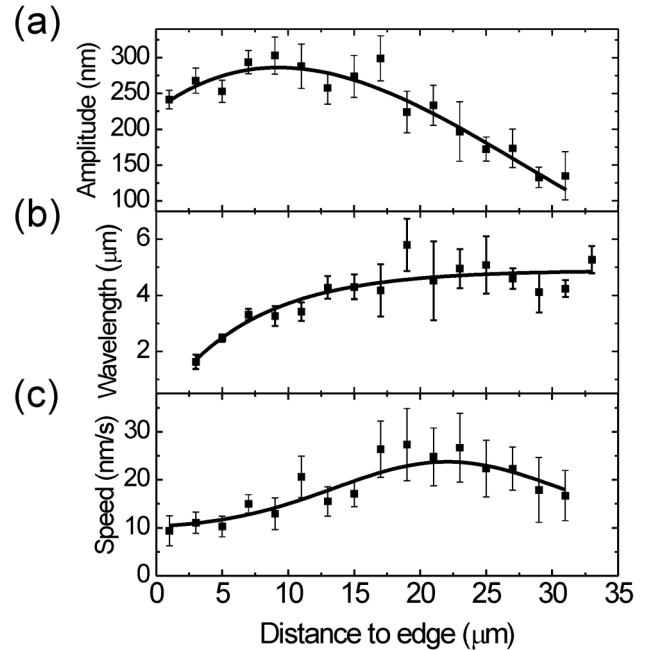


FIG. 2. (a) Peak-to-valley amplitudes of membrane waves versus the distances to cell edges. Solid curve is a guide to the eye. (b) Wavelengths versus the distances to cell edges. Solid curve is a fitting of $\lambda(x) = \lambda_a[1 - \exp(-x/x_c)]$. (c) Wave speeds versus the distances to cell edges. Solid curve is a guide to the eye. Each data point represents the mean in a $2\text{-}\mu\text{m}$ distance interval, and the horizontal values are the centers of intervals. The error bars are 95% confidence intervals determined by Student's t distribution.

$7.0\ \mu\text{m}$. The wavelengths reach 72% the steady-state value after $9\ \mu\text{m}$ of propagation, but the energy dissipation caused by the viscosities of the surrounding medium and the cytoplasm starts to reduce the amplitudes at this distance. We also show the propagating speeds v of the wave peaks along the distance in Fig. 2(c). Because most of the waves were recorded on protruding lamellipodia, the speeds are calculated relative to the cell edges. The values of speeds are within the same order of magnitude as those measured by bead movements on cell membranes [3]. The speeds are small at the edges, reach a maximum and then start to decrease at about $23\ \mu\text{m}$. This trend is in agreement with a recent numerical study of the retrograde actin-myosin flow in lamellipodia [17].

Figure 3(a) shows the dispersion relation of the membrane waves. The angular frequency of membrane waves is defined as $\omega = 2\pi v/\lambda$. We compare the measured dispersion relation with the active membrane wave model [9,10]. In brief, this model considers the membrane wave as a result of the interactions among the protrusion force of actin polymerization, the contraction force produced by myosin, and the membrane tension as well as the bending modulus. In the frequency domain, this membrane-actin-myosin system is described by the following equations of motion in a matrix form:

$$(M + i\omega I) \begin{pmatrix} h(q, \omega) \\ m(q, \omega) \\ n(q, \omega) \end{pmatrix} = \begin{pmatrix} f_0 \delta(\omega - \omega_0) \\ 0 \\ 0 \end{pmatrix}, \quad M = \begin{pmatrix} \hat{O}(-\kappa q^4 - \sigma q^2 - \gamma) & -\hat{O}A^* & \hat{O}(A - \kappa \bar{H} q^2 / n_0) \\ 0 & -k_{\text{off}} & k_{\text{on}} \\ -\Lambda \kappa \bar{H} q^4 & 0 & -Dq^2 \end{pmatrix}, \quad (1)$$

where q is the wave number, h is the membrane height, m is the local density of attached myosin motors, n is the local density of actin nucleators, \hat{O} is the Oseen tensor, κ and σ are the bending modulus and the surface tension of the membrane, γ is a coefficient for local elastic restoring force, \bar{H} and Λ are the spontaneous curvature and the mobility of the actin nucleators, n_0 is the average density of the actin nucleators, A and A^* are the actin protrusive and myosin contractile force coefficients, f_0 and ω_0 are the amplitude and angular frequency of the driving force, k_{on} and k_{off} are the myosin-actin binding and unbinding rates, D is the diffusion constant for actin nucleators, and I is the identity matrix. The Oseen tensor can also be represented as $\hat{O} = d/4\eta$, where d is a fluid confinement length in the actin-filament network and η is the average viscosity of the cytoplasm. Solving the eigenvalue equation of the matrix M , one may obtain the dispersion relation $\omega(q)$.

The fitting result by the theoretical dispersion relation is shown as the solid curve in Fig. 3(a). The variable parameters used for this fitting are k_{off} , A , and A^* , because they are most effective to control the deviations between experimental data and theoretical values. Other parameters are

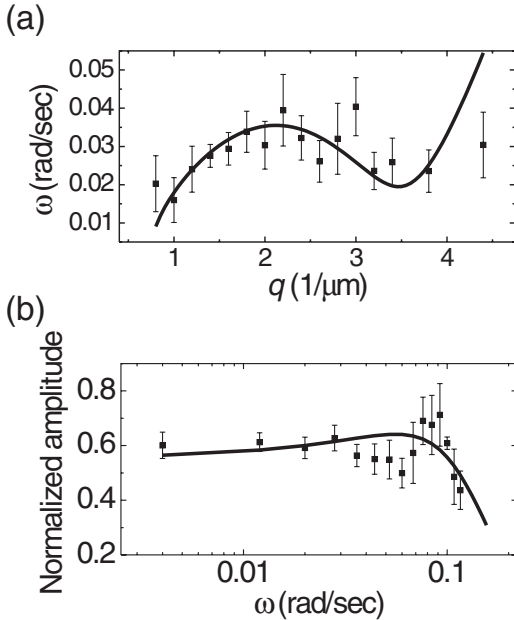


FIG. 3. (a) Dispersion relation of membrane waves. Each data point represents the mean in a wave-number interval of $0.2 \mu\text{m}^{-1}$. (b) Frequency response of the peak-to-valley amplitudes, normalized to the maximum values of each cell. Each data point represents the mean in an angular-frequency interval of 0.008 rad/sec . The error bars are 95% confidence intervals determined by Student's t distribution. The fitting curves are based on the active membrane wave model. For details, please see the text.

mostly collected from Ref. [9], and listed in Table I. For the fitting curve in Fig. 3(a), $k_{\text{off}} = 0.030 \text{ sec}^{-1}$, $A = 7.0 \times 10^{-5} \text{ g } \mu\text{m}^2/\text{sec}^2$, and $A^* = 3.7 \times 10^{-9} \text{ g } \mu\text{m}^2/\text{sec}^2$. The chi-square value of this fitting is 17.97, corresponding to a goodness-of-fit estimation of 0.16 calculated by using the incomplete gamma function [18]. The fitting curve is close to the data points except the one at the largest q (shortest wavelength) in our measurement. Because the shortest wavelengths occur at the cell edges, we suspect that the concentrations of involved proteins may be lower than those in the rear parts of lamellipodia, and therefore the membrane cannot support high-frequency waves as predicted by the model. Otherwise, the data verify that the active membrane model correctly depicts the dispersion of membrane waves.

Equation (1) also gives the frequency response of amplitudes. In this modeling we use the maximum amplitude of each cell to normalize the measured membrane amplitudes. The experimental data in Fig. 3(b) demonstrate that the amplitudes decay dramatically for the angular frequency higher than 0.092 rad/sec . One major difference between the active membrane model and the data in Fig. 3(b) is that the model specifies the frequency response of normalized amplitudes at a specific distance from the driving source, but our data are statistical results acquired at various distances to the cell edges. For calculating the curve in Fig. 3(b), we set the distance from the driving source as $8 \mu\text{m}$, larger than the characteristic distance x_c ($7.0 \mu\text{m}$). Other variables used to generate the curve are $k_{\text{off}} = 0.009 \text{ sec}^{-1}$, $A = 3 \times 10^{-8} \text{ g } \mu\text{m}^2/\text{sec}^2$, and $A^* = 5 \times 10^{-8} \text{ g } \mu\text{m}^2/\text{sec}^2$. The curve in Fig. 3(b) is thus considered as a qualitative description of the frequency response for amplitudes. Nevertheless, the active membrane

TABLE I. List of the parameters used for calculating the curves in Fig. 3. For the parameters with two values, the first is used in Fig. 3(a), and the second is used in Fig. 3(b).

Parameter	Value
$\kappa [k_B T]$	0.75, 2.5
$D [\mu\text{m}^2/\text{sec}]$	1
$\eta [\text{g}/\mu\text{m}\text{-sec}]$	10^{-4}
$\bar{H} [\mu\text{m}^{-1}]$	-50
$\Lambda [\text{sec}/\text{g}]$	10^4
$n_0 [\mu\text{m}^{-2}]$	5×10^3
$d [\mu\text{m}]$	0.1
$\sigma [k_B T/\mu\text{m}^2]$	2.5, 25
$\gamma [k_B T/\mu\text{m}^4]$	75, 37.5
f_0	1
$k_{\text{on}} [\text{sec}^{-1}]$	300

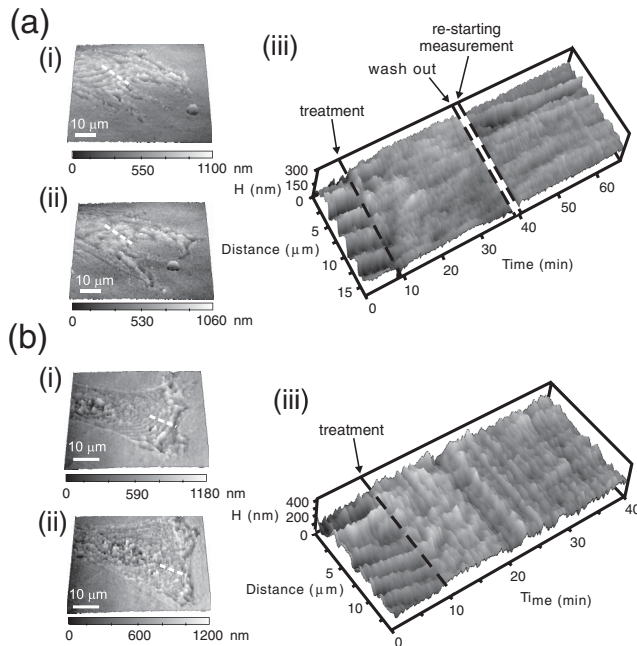


FIG. 4. (a) Membrane topography of a cell (i) before and (ii) 23 min after the treatment of 75 μ M BBI. (iii) Kymograph of the membrane topography. We treated the cell at the 9th min, washed out the reagent at the 39th min, and restarted the measurement at the 41st min. (b) Membrane topography of a cell (i) before and (ii) 25 min after the treatment of 100 nM LA. (iii) Kymograph of the membrane topography.

model correctly depicts the decay of amplitudes for ω higher than 0.1 rad/sec.

As a verification of the driving mechanisms of membrane waves, we use reagents to suppress the activities of myosin II and actin polymerization. In these experiments we used as low concentrations as possible such that the cell morphology was not varied dramatically but the membrane waves showed significant differences. Figure 4(a) shows the results with the treatment of blebbistatin (BBI), which is known to inhibit the activities of myosin II through the suppression of the adenosine triphosphatase, and this effect is reversible [19]. In the kymograph of Fig. 4(a), the waves disappear right after the treatment of 75 μ M BBI. After we wash out the BBI, a peak of the membrane wave recovers from the edge in two minutes, showing the reversible effect of BBI. We also treat another cell with latrunculin A (LA) that binds to actin monomers and impedes actin polymerization [20]. In Fig. 4(b) the membrane waves are flattened by the treatment of 100 nM LA. This result implies that the membrane elevation or edge ruffling is supported by actin polymerization, consistent with the model of membrane waves proposed by Giannone *et al.* [8]. We also repeat the measurement with lower concentrations of LA. At 75 nM, the waves are sustained with amplitudes being reduced by 15%–20%, while the speeds of waves are decreased by

70%–80%. It seems that the propagation speeds are more sensitive to the treatment of LA. However, the results with 50 nM LA exhibit large variations among individual cells. The responses of some cells are not obvious. Further systematic investigations are necessary to reveal the dependence of membrane wave propagation characteristics on reagent concentrations.

In conclusion, we use the NIWOP technique to study the dynamics of active membrane waves on fibroblasts. The kymographs of membrane topography provide direct validation of existing models about the waves. The measured dispersion relation and frequency response of amplitudes are both close to the descriptions of the active membrane model proposed by Shlomovitz and Gov. The treatment with either blebbistatin or latrunculin A suppresses the membrane waves effectively, verifying that the contractile force of myosin II and the protrusion force from actin polymerization are both required for the generation of membrane waves.

We thank Roie Shlomovitz and Nir S. Gov for useful discussions. This work is financially supported by the National Science Council of Taiwan (Contract NSC 97-2112-M-001-022-MY3) and the Academia Sinica Research Program on Nanoscience and Nanotechnology.

*clee@gate.sinica.edu.tw

- [1] B. Hinz *et al.*, *Exp. Cell Res.* **251**, 234 (1999).
- [2] R. Buccione, J.D. Orth, and M.A. McNiven, *Nat. Rev. Mol. Cell Biol.* **5**, 647 (2004).
- [3] G. Giannone *et al.*, *Cell* **116**, 431 (2004).
- [4] B. Borm *et al.*, *Exp. Cell Res.* **302**, 83 (2005).
- [5] C.-C. Wang, J.-Y. Lin, and C.-H. Lee, *Opt. Express* **13**, 10665 (2005).
- [6] H.-G. Dobreiner *et al.*, *Phys. Rev. Lett.* **97**, 038102 (2006).
- [7] C.-C. Wang *et al.*, *Opt. Lett.* **31**, 2873 (2006).
- [8] G. Giannone *et al.*, *Cell* **128**, 561 (2007).
- [9] R. Shlomovitz and N.S. Gov, *Phys. Rev. Lett.* **98**, 168103 (2007).
- [10] R. Shlomovitz and N.S. Gov, *Phys. Rev. E* **78**, 041911 (2008).
- [11] G. Popescu *et al.*, *Opt. Lett.* **31**, 775 (2006).
- [12] J.C. Neto *et al.*, *Biophys. J.* **91**, 1108 (2006).
- [13] C.-H. Lee, H.-Y. Mong, and W.-C. Lin, *Opt. Lett.* **27**, 1773 (2002).
- [14] M.A.A. Neil, R. Juskaitis, and T. Wilson, *Opt. Lett.* **22**, 1905 (1997).
- [15] C.H. Lee and J. Wang, *Opt. Commun.* **135**, 233 (1997).
- [16] C.-C. Wang *et al.*, *Microsc. Res. Tech.* **71**, 594 (2008).
- [17] B. Rubinstein *et al.*, *Biophys. J.* **97**, 1853 (2009).
- [18] W.H. Press *et al.*, *Numerical Recipes in C* (Cambridge University Press, Cambridge, England, 1992), 2nd ed., Chap. 15.
- [19] A.F. Straight *et al.*, *Science* **299**, 1743 (2003).
- [20] E.G. Yarmola *et al.*, *J. Biol. Chem.* **275**, 28120 (2000).